Rapidity dependence of deuteron production in central Au + Au collisions at $\sqrt{s_{NN}} = 200$ GeV

I. Arsene,[11,*] I. G. Bearden,[5] D. Beavis,[1] S. Bekele,[10,†] C. Besliu,[9] B. Budick,[3] H. Bøggild,[5] C. Chasman,[1] C. H. Christensen,[5] P. Christiansen,[5,‡] H. H. Dalsgaard,[5] R. Debbe,[1] J. J. Gaardhøje,[5] K. Hagel,[7] H. Ito,[1] A. Jipa,[9] E. B. Johnson,[10,§] C. E. Jørgensen,[5,‖] R. Karabowicz,[4] N. Katrynska,[4] E. J. Kim,[10,¶] T. M. Larsen,[5] J. H. Lee,[1] G. Løvhøiden,[11] Z. Majka,[4] M. Murray,[10] J. Natowitz,[7] B. S. Nielsen,[5] C. Nygaard,[5] D. Pal,[10] A. Qviller,[11] F. Rami,[2] C. Ristea,[5] O. Ristea,[9] D. Röhrich,[8] S. J. Sanders,[10] P. Staszel,[4] T. S. Tveter,[11] F. Videbæk,[1,**] R. Wada,[7] H. Yang,[8,††] Z. Yin,[8,‡‡] and S. Zgura[6]

[1]*Brookhaven National Laboratory, Upton, New York 11973-5000, USA*
[2]*Institute Pluridisciplinaire Hubert Curien CRNS-IN2P3 et Université de Strasbourg, Strasbourg, France*
[3]*New York University, New York, New York 10003, USA*
[4]*Smoluchowski Inst. of Physics, Jagiellonian University, Krakow, Poland*
[5]*Niels Bohr Institute, Blegdamsvej 17, University of Copenhagen, Copenhagen, Denmark*
[6]*Institute for Space Sciences, Bucharest, Romania*
[7]*Texas A&M University, College Station, Texas 17843, USA*
[8]*University of Bergen, Department of Physics and Technology, Bergen, Norway*
[9]*University of Bucharest, Bucharest, Romania*
[10]*University of Kansas, Lawrence, Kansas 66045, USA*
[11]*University of Oslo, Department of Physics, Oslo, Norway*
(BRAHMS Collaboration)

(Received 28 May 2010; revised manuscript received 10 December 2010; published 18 April 2011)

We have measured the distributions of protons and deuterons produced in the 20% most central Au + Au collisions at the Relativistic Heavy-Ion Collider (RHIC) ($\sqrt{s_{\rm NN}} = 200$ GeV) over a very wide range of transverse and longitudinal momentum. Near midrapidity we have also measured the distribution of antiprotons and antideuterons. We present our results in the context of coalescence models. In particular, we extract the "homogeneity volume" and the average phase-space density for protons and antiprotons. Near central rapidity the coalescence parameter $B_2(p_T)$ and the space-averaged phase-space density $\langle f \rangle(p_T)$ are very similar for both protons and antiprotons. For protons we see little variation of either $B_2(p_T)$ or the space-averaged phase-space density as the rapidity increases from 0 to 3. However, these quantities depend strongly on p_T at all rapidities. These results are in contrast to data from lower-energy collisions where the proton and antiproton phase-space densities are different at $y = 0$, and both B_2 and $\langle f \rangle$ depend strongly on rapidity.

DOI: 10.1103/PhysRevC.83.044906 PACS number(s): 25.75.Gz, 13.85.−t, 25.40.Ve, 25.75.Ld

I. INTRODUCTION

Deuterons detected in heavy-ion collisions are conventionally thought to be produced predominantly via a process called coalescence. Protons and neutrons that are close enough in phase-space (i.e., in position and momentum space) "coalesce" to form deuterons. The surrounding medium created in the $A + A$ collisions enables this "$2 \rightarrow 1$" process to proceed while conserving energy and momentum. There is a wide range of evidence to suggest that a dense system of strongly interacting partons is created in heavy-ion collisions at Relativistic-Heavy-Ion-Colider (RHIC) energies [1]. In the hot and dense system produced in high-energy ion collisions, the coalescence of nucleons into deuterons cannot even begin before the the partons have frozen out into hadrons. Even then, the low binding energy of deuterons (∼2.2 MeV), ensures that only deuterons produced late will survive to reach the detectors. Thus, our sample is dominated by deuterons produced close to thermal freeze-out, where the nuclear density is low [2,3].

Early coalescence models assumed that the phase-space density of clusters is proportional to the product of the phase-space densities of individual nucleons which they coalesced and that the momentum of the deuteron is trivially the sum of the nucleon momenta [4–6]. More recent coalescence models add insight into the nature of the phenomenon, but still relate cluster production to the product of phase-space densities [7]. For deuterons this is written as

$$E_d \frac{d^3N_d}{dp_d^3} = B_2(\mathbf{p}) \left(E_p \frac{d^3N_p}{dp_p^3} \right)^2, \quad (1)$$

[*]Present Address: ExtreMe Matter Institute EMMI, GSI, Darmstadt, Germany
[†]Present address: Dept. of Physics, Tennessee Tech University, Cookeville, Tennessee, USA
[‡]Present Address: Div. of Experimental High-Energy Physics, Lund University, Lund, Sweden
[§]Present address: Radiation Monitoring Devices, Cambridge, Massachusetts, USA
[‖]Present address: Risø National Laboratory, Denmark
[¶]Present address: Division of Science Education, Chonbuk National University, Jeonju, 561-756, Korea
[**]Spokesperson
[††]Present address: University of Heidelberg, Heidelberg, Germany
[‡‡]Present address: Institute of Particle Physics, Huazhong Normal University, Wuhan, China

where **p** is the momentum of the proton and B_2 is defined as the coefficient linking the square of the nucleon distribution to that of the proton distribution.

Ideally for a coalescence study one would measure the spectra of both protons and neutrons. At $\sqrt{s_{\rm NN}} = 4.9$ GeV the n/p ratio measured in the 10% most central Au on Pb collisions has a value of $1.19 \pm .08$ and is independent of m_T in a wide range of rapidity (1.6 to 2.4) [8], whereas the same ratio for the incident nuclei is equal to 1.52. (Measurements by other experiments imply that most of the isospin lost by the neutrons goes into an excess of π^- over π^+ [9,10].) At higher energies we expect n/p to be close to 1 over a wide rapidity range.

In thermodynamic models that assume a thermalized distributions of nucleons, B_2 carries information about the effective volume (in coordinate space) of the nucleons when they coalescence. This is also known as the homogeneity volume, and is defined as the volume over which nucleons are close enough in momentum that they can coalesce [4–6]. At RHIC, the homogeneity volume of the emitting source has been studied in great detail at central rapidity but few measurements are available in the forward region. Consequently, the deuteron coalescence analysis gives BRAHMS a unique opportunity to study the volume of the proton source over a wide range of rapidity.

The paper is organized as follows: This introduction continues with a short review of the homogeneity volume and the phase-space density averaged over coordinate space. Section II details the detector setup, the selection of the central events used for this analysis, the tracking algorithm, particle identification, and the feed-down corrections applied to the proton and antiproton spectra. In Sec. III we describe the fully corrected spectra and the inferred values of B_2 and average phase-space density as functions of transverse momentum and rapidity. Finally, we summarize our results and the physics that we extract from them.

A. B_2 and the homogeneity volume

The link between B_2 and the homogeneity volume can be seen in coalescence models that use the so-called sudden approximation technique to write the phase-space density of deuterons as an overlap of the nucleon wave functions with the deuteron wave function. The volume of the nucleon system is introduced through the normalization of their wave functions [11]. One can make a reasonable approximation of the deuteron's wave function by assuming it is a Gaussian of width $\delta = 2.8$ fm. If we further assume that the region where coalescence occurs also has a Gaussian spatial profile with width R_G, one can write [12]

$$\left(R_G^2(\mathbf{p}) + \frac{\delta^2}{2}\right)^{3/2} = \frac{3}{2}\frac{\pi^{3/2}\hbar^3}{B_2(\mathbf{p})m_p c^2}, \tag{2}$$

where m_p denotes the proton mass. The left-hand side of this equation just represents the convolution of the proton source size and the Gaussian representation of the deuteron wave function. For small systems, δ dominates over R_G and the measurements have only little sensitivity to the proton source size. One advantage of this ansatz is that it facilitates comparison to interferometry radii. We show in Sec. III that this model works well for our data since we find consistency between our estimate of the proton source size and Hanbury Brown-Twiss (HBT) results. At lower beam energies, R_G has been found to be very consistent with radii measured from $\pi\pi$, KK, and pp correlations [13]. The deuteron wave function is more accurately represented by the Hulthen form, which has an exponential tail [14]. For the B_2 values reported in this paper the error in R_G from using Eq. (2) is less than 0.2 fm [13].

For a variety of ion beams ranging from He to Ar incident on nuclear targets at BEVALAC energies [15], as well as $p + A$ fixed-target experiments at the Fermi National Accelerator Laboratory (FNAL) [16], Japan's National Laboratory for High Energy Physics (KEK) [17], and at the CERN Super Proton Synchrotron (SPS) [18], the measured B_2 values are independent of energy and p_T, and are consistent with measurements of the spatial parameters of the deuteron wave function. At higher $A + A$ energies, including the BNL Alternating Gradient Synchrotron (AGS) Au + Au fixed-target $\sqrt{s_{\rm NN}} = 4.9$ GeV [19–24], the SPS S + S, S + Pb and Pb + Pb at $\sqrt{s_{\rm NN}} \approx 18$ GeV [25–27], and Au + Au ($\sqrt{s_{\rm NN}} = 200$ GeV) at the RHIC collider [28–30], B_2 decreases with energy and increases with p_T. This is consistent with the formation of deuterons in an expanding medium [31–33]. Near midrapidity B_2 decreases by a factor of ≈20 as the center-of-mass energy increases from $\sqrt{s_{\rm NN}} \approx 1$ to 17.3 GeV [26] before flattening out at RHIC energies [34,35]. This is similar to the behavior seen in HBT radii [36,37].

B. Average phase-space density

The average of the phase-space density $f(\mathbf{x}, \mathbf{p})$ over the system volume at freeze-out time is a quantity which, when compared to Bose-Einstein or Fermi-Dirac statistics, allows the assessment of the degree of chemical or kinetic equilibrium reached by the system at that stage [38,39]. This quantity also carries information about the possible multiple-particle symmetrization effects (i.e., pion condensates). Values greater than 1.0 would indicate the presence of quantum effects [38]. This quantity is a count of the states that the system can occupy and, as such, is used to define the contribution of particular types of particles to the overall entropy of the system. The spatial average of the phase-space density is defined as the following ratio:

$$\langle f \rangle(\mathbf{p}) \equiv \frac{\int d^3x f^2(\mathbf{x}, \mathbf{p})}{\int d^3x f(\mathbf{x}, \mathbf{p})}, \tag{3}$$

where the integration is carried out over spatial coordinates bound by the homogeneity volume of the system at freeze-out. The formal definition of phase-space density $f(\mathbf{x}, \mathbf{p})$ for a particle of spin J is written as

$$f(\mathbf{x}, \mathbf{p}) \equiv \frac{(2\pi\hbar)^3}{(2J+1)}\frac{d^6N}{dp^3dx^3}. \tag{4}$$

For a system in chemical equilibrium at temperature T and chemical potential μ,

$$f(E) = \frac{1}{e^{(E-\mu)/T} \pm 1}, \tag{5}$$

where E is the energy and ± 1 selects bosons or fermions, respectively. For a dilute system, (i.e., $f \ll 1$), Eq. (5) gives

$$f_d \approx e^{-(E_d - \mu_p - \mu_n)/T}. \tag{6}$$

Since $E_d = m_T \cosh(y)$, one would expect the phase-space density to be an exponential in m_T. Note that, in this simple derivation, we are ignoring the collective motion of the particles. At $\sqrt{s_{\rm NN}} = 17.3$ GeV, it was found that strong longitudinal flow could significantly reduce the space-averaged phase-space density of pions [40]. Also, at this energy the inverse slope of the phase-space density was found to increase with particle mass in a manner suggestive of transverse flow [41]. Using the fact that the deuteron has energy $E_d = E_n + E_p$ and momentum $\mathbf{P} = 2\mathbf{p}$, Eq. (6) implies that

$$f_d(\mathbf{x}, \mathbf{P}) = f_p(\mathbf{x}, \mathbf{p}) f_n(\mathbf{x}, \mathbf{p}) = f_p^2(\mathbf{x}, \mathbf{p}). \tag{7}$$

To extract the average phase-space density of protons one can then replace the squared term in the numerator of Eq. (3) by the phase-space density of deuterons:

$$\langle f_p \rangle(\mathbf{p}) = \frac{1}{3}\left(E_d \frac{d^3N_d}{dp_d^3}\right) \Big/ \left(E_p \frac{d^3N_p}{dp_p^3}\right). \tag{8}$$

Furthermore, one can make use of the assumption that deuterons are formed by coalescence and satisfy Eqs. (1) and (2) to obtain an expression for the average phase space of protons, similar to what Bertsch originally suggested for pions. Dividing the spectrum by the product of the HBT radii gives [38,39]

$$\langle f_p \rangle(\mathbf{p}) = \frac{1}{2} E_p \frac{d^3N_p}{dp^3} \frac{\pi^{3/2}\hbar^3}{R_G^3(\mathbf{p}) m_p c^2}. \tag{9}$$

The phase-space densities calculated using Eq. (8) have the expected exponential dependence in m_T. When using Eq. (9), one introduces the assumption that deuterons are produced via coalescence and that the homogeneity volume extracted from deuteron distributions is also the volume of the proton source. The calculation of the space-averaged phase-space density of protons using these assumptions is close in value to the one obtained from an assumed thermal equilibrium and has the same behavior in m_T. This suggests that the system has evolved into chemical equilibrium at freeze-out. While chemical equilibrium has been very well established at RHIC energies for the system at midrapidity, these data allow us to test if the matter at forward rapidity also reaches equilibrium. To ease the comparison with lower-energy data we have decided to use Eq. (8) to calculate the phase density.

The coalescence parameter B_2 and the space-averaged phase-space density recast the information contained in the proton and deuteron spectra into "dynamic" and "chemical" terms. The coalescence parameter B_2 can be interpreted in terms of the volume of homogeneity, which depends upon the temperature of the system and the radial flow. Indeed, one confirmation that we are actually seeing coalescence would be to see if this radius was consistent with the appropriate HBT radii. This was checked at $\sqrt{s_{\rm NN}} = 17.3$ GeV by comparing R_G to radii extracted from $\pi\pi$, KK, and pp correlation measurements [13,42–44]. In this paper, we use the very large angular and momentum ranges of the two BRAHMS spectrometers to measure the rapidity dependence of the volume of homogeneity and space-averaged phase-space density of the (anti)proton distributions for central Au + Au collisions.

II. ANALYSIS

The data in this paper were collected by the BRAHMS experiment in 2004. We present proton and deuteron spectra at $\sqrt{s_{\rm NN}} = 200$ GeV Au + Au collisions with a centrality range of 0%–20%. The statistics for deuterons at high rapidity for more peripheral data are limited, so a centrality-dependence analysis was not warranted. The data are analyzed in four rapidity bins: (−0.1, 0.1), (0.5, 1.2), (1.5, 2.5), and (2.8, 3.2). We have also measured antiproton and antideuteron spectra at $y \approx 0$ and $y \approx 0.8$.

A. Detector system

The BRAHMS experimental setup consists of two movable magnetic spectrometers, the forward spectrometer (FS) that can be rotated from 2.3° to 15°, and the midrapidity spectrometer (MRS) that can be rotated from 90° to 30° degrees relative to the beamline. Fast Cherenkov counters at high rapidities were used to measure luminosity, to determine the interaction vertex, and to provide a start time for time-of-flight measurements.

The MRS has two time projection chambers (TPCs), TPM1 and TPM2, situated in field-free regions in front and behind a dipole magnet. This assembly is followed by a highly segmented scintillator time-of-flight (TOF) wall at 4.51 m. The FS consists of 4 dipole magnets D1, D2, D3, and D4 with a total bending power of up to 9.2 Tm. The spectrometer has 5 tracking stations T1 through T5. T1 and T2 are TPCs placed in front of and after the second dipole D2. T3, T4, and T5 are drift chambers with T3 in front of D3, T4 between D3 and D4, and T5 after D4 and just in front of the ring-imaging Cherenkov (RICH) [45]. Details on the BRAHMS experimental setup can be found in Ref. [46].

B. Centrality selection

The centrality of the collisions at the BRAHMS interaction region was extracted from charged-particle multiplicity densities measured with a multiplicity array (MA). The MA consists of a coaxial arrangement of Si strip detectors and scintillator tiles surrounding the intersection region [47]. The pseudorapidity coverage of the MA is approximately $-2.2 < \eta < 2.2$. The centrality selection is derived from minimum-bias trigger events, which are defined using two zero-degree calorimeters (ZDCs), requiring an energy deposit equivalent to at least one neutron in each of the two detectors and also requiring a signal in the MA in order to reject Coulomb dissociation events [46,48]. The uncertainty in the centrality determination from our multiplicity distributions is estimated to be ±4% of the size of the bin for the 0%–20% bin. The fraction of the inclusive yield lost by the minimum-bias trigger is estimated to be about 4% and was corrected for.

C. Tracking

Track reconstruction starts by finding local track segments in the TPCs and (for the FS) in the drift chambers. These

detectors are in field-free regions and so these local tracks are straight lines. Local tracks on either side of a magnet are matched using the effective edge approximation generating what we call locally matched tracks. The locally matched tracks are then combined in the FS to form complete tracks. The complete tracks are refitted to extract the best measurement of the particle three-momentum. Tracks in the FS are required to project through the magnet D1 onto the nominal beamline. Track quality cuts are applied for the final track selection. The momentum resolution at full field (where all data presented in this paper were taken) is $\delta p/p = 0.0008p$.

The momentum distributions are corrected for tracking-detector efficiency and geometrical acceptance. Tracking and matching efficiencies for each of the 5 tracking stations in the FS were calculated by constructing full tracks using just four track segments and evaluating the efficiency in the fifth station by comparing the predicted position and direction of the interpolated or extrapolated full track in that station with the known local segments. The local track efficiency was evaluated as a function of spectrometer angle and field setting, as well as of position and direction of the local track segments. The overall tracking efficiency is typically 60% and is known to a few percent. In the MRS the tracking efficiencies are determined from Monte Carlo simulation using embedding techniques. The systematic error is below 4%. We correct for absorption, multiple scattering, and energy loss in the detectors using GEANT 3.21 [49]. The magnitude of these corrections on the particle yields depends on the particle momenta and the spectrometer positions and, in the FS, it is about 20% with an estimated uncertainty of 2%. In the MRS the corrections are less than 8% with a small systematic error. We assume that deuteron absorption factorizes from other effects and model it as the square of the proton absorption correction (at $p_T/2$) as done in Ref. [13]. More details about tracking in the MRS can be found in Ref. [50].

D. Particle identification

In the midrapidity region, particle identification is done using time-of-flight measurements, while at forward rapidities we use the RICH [45]. At $y = 0$ and 0.8 we select (anti)protons using a 3σ cut on $m^2 = p^2(\frac{c^2L^2}{t^2} - 1)$, where L is the length of the path followed by a particle, t its time of flight, and c is the speed of light. For deuterons, a simple 3σ cut around the (anti)deuteron mean mass is used. These deuteron yields are corrected for background that arises from false matching of tracks with background hits in the TOF wall. This background is determined from data in the mass region outside the deuteron peak, and contributes to the systematic error of the deuteron yields by ∼5%–10%, decreasing with p_T. At forward rapidities the RICH provides proton and deuteron PID separation. The ring radius R in the RICH depends on the particle's velocity. For a particle of mass m in the RICH, $R \approx 9.2[1 - (p/p_{\text{thres}})^2]$ cm where $p_{\text{thres}} = 16.1mc$. The PID performance is shown in Fig. 1, where the bands represent the limits used for the analysis. Because of inefficiencies, about 3% of the particles moving faster than their Cherenkov threshold do not produce an identified ring. Protons and deuterons with momenta between the kaon and proton thresholds do not make a ring. The contamination from misidentified kaons and pions are subtracted to deduce the proton spectrum in this momentum range (neglecting the small fraction of deuterons). The contamination correction to the proton spectrum is ∼10% at $p_T = 0.5$ GeV/$c$and drops to ∼2% at $p_T = 1.5$ GeV/c. The error on this correction is negligible. This procedure cannot be used in the region between the proton and deuteron thresholds since the contamination from pions, kaons, and protons dominates the small deuteron yield.

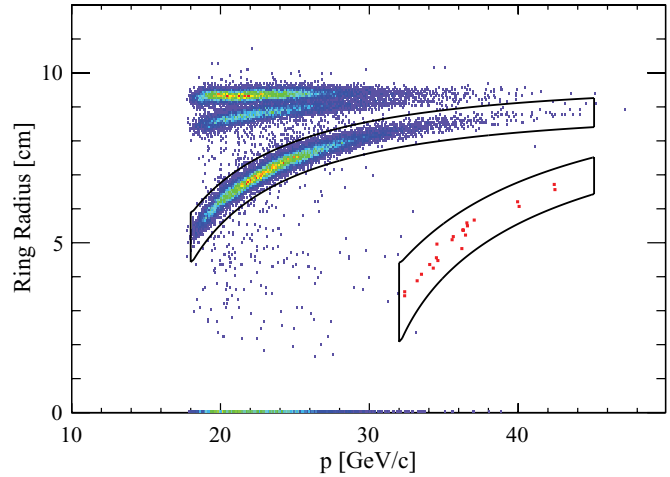

FIG. 1. (Color online) Ring radius versus momentum for particles at $y \approx 3$ showing the pion, kaon, proton, and deuteron separation. The bands show the proton and deuteron selection used in the analysis.

E. Feed-down corrections

We have corrected our data to account for the hyperons that decay into protons using the method described in [51]. The correction factor C is given by

$$C = \frac{N_p}{N_p + N_\Lambda + N_{\Sigma^+}}, \tag{10}$$

where N_p is the number of primary protons and N_Λ and and N_{Σ^+} are the number of protons coming from Λ and Σ^+ decay, respectively. Near central rapidity we have used the Λ spectra measured by PHENIX [52] and estimated the Σ/Λ ratio from lower-energy measurements [51]. Since there are no measurements of Λs at forward rapidities we have estimated the Λ/p ratio based on thermal models that were fitted to the rapidity densities of charged pions, kaons, protons, and antiprotons measured by BRAHMS in the forward region [53].

With our model calculations, we find that the ratio $\frac{dN_\Lambda}{dy}/\frac{dN_p}{dy}$ varies slowly with rapidity up to rapidities $y \approx 4$. The systematic error from uncertainties on the yields and the model extrapolation is estimated to be less than 3%. The correction factor also depends on the p_T dependence of the Λ/p ratio. BRAHMS has found that the mean transverse kinetic energy scales linearly with the mass of the particle with a slope that depends only weakly on rapidity [54]. We have used these systematics to estimate the inverse slope T

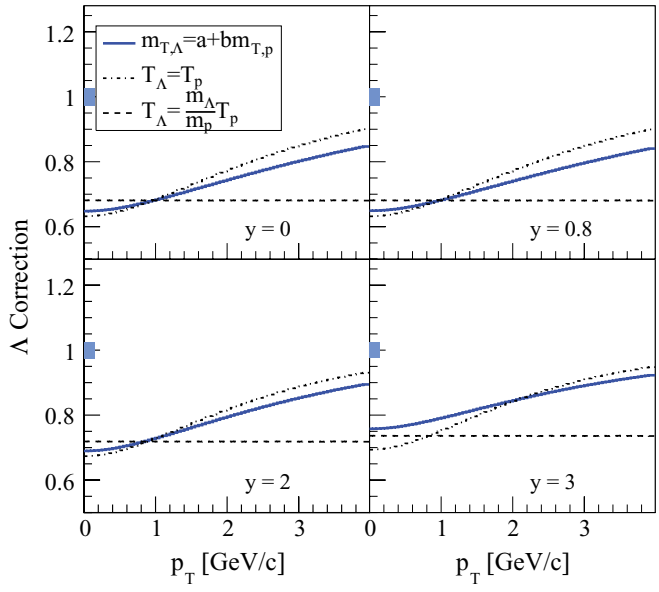

FIG. 2. (Color online) p_T-dependent feed-down correction factors for protons versus p_T and rapidity. The three sets of lines show the effect of various scenarios for the difference in shape between proton and Λ spectra. Systematic errors on the correction due to uncertainties in the yield ratio of protons and Lambdas are shown by the bands to the left of the plots. The curves for antiprotons are very similar.

of the Λ m_T distribution. To estimate the systematic error in the p_T dependence of the correction factor we have taken the limiting cases of $T_\Lambda = T_p$ and $T_\Lambda = T_p(m_\Lambda/m_p)$. This produces an error in the correction factor that is almost zero at $p_T = 1\,\mathrm{GeV}/c$ and reaches −9%, +6% at $p_T = 2\,\mathrm{GeV}/c$. The correction factor as a function of p_T and rapidity is shown in Fig. 2. It varies only weakly with rapidity and has a systematic error that is small in comparison to the statistical errors on B_2 and the space-averaged phase-space density. At $p_T = 2\,\mathrm{GeV}/c$ the total error from the feed-down correction reaches a value of 19% for B_2 and 10% for the space-averaged phase-space density.

III. RESULTS

Figure 3 shows the invariant proton and deuteron spectra versus p_T for the four measured rapidity bins. The systematic error on the normalization of the spectra is estimated to be about 5% with a point-to-point error in the spectra of ≈8% arising from the merging of spectrometer settings and PID and uncertainties in tracking-efficiency determination. We fit exponentials in m_T to the spectra and extract the invariant yields, dN/dy, and inverse slopes T. These are listed in Table I. About 40%– 50% (dependent on rapidity) of the yield of the deuterons is contained within our acceptance. For protons the fractions are slightly higher: 55%–60%. The proton yield falls slightly from $y = 0$ to $y = 3$, but no firm conclusion can be made for the deuterons due to the limited p_T range at high rapidity. The inverse slopes tend to decrease with rapidity, suggesting a decrease of radial flow. The inverse slopes of the deuterons are somewhat higher than those of the protons. The average over all rapidities for the ratio of the inverse slopes is 1.6 ± 0.1. For antideuterons the inverse slopes are a factor of 2.0 ± 0.2 higher than that of antiprotons.

Figure 4 shows B_2 versus p_T and rapidity. B_2 increases with p_T, which is consistent with previous experiments [26,35]. Using Eq. (2), we find that, at central rapidity, the source radius R_G falls from 4.2 ± 0.2 fm to 3.1 ± 0.4 fm as m_T increases from 1.2 to 1.9 GeV/c^2. This is consistent with the m_T dependence of HBT radii, $R \propto 1/\sqrt{m_T}$, that has been observed by PHENIX [36] and STAR [37] and also at SPS energies [43]. The solid line in each rapidity panel represents an exponential fit to our data at $y = 0$. We see no evidence of any rapidity dependence of $B_2(p_T)$. The proton and antiproton B_2 values are very close at this energy, implying a similar source size. This is in contrast to the measurements at $\sqrt{s_{\mathrm{NN}}} =$ 17.3 GeV where the antiproton source volume was found to be somewhat larger than the proton source volume [13].

Figure 5 shows the average phase-space density $\langle f \rangle(m_T)$ for protons and antiprotons as a function of rapidity. These values are calculated using Eq. (8). The space-averaged phase-space density decreases as m_T increases, as expected from Eq. (5). The solid curve in each panel of Fig. 5 is a exponential fit to the proton density at $y = 0$. We see little rapidity dependence of $\langle f \rangle(p_T)$.

From Eq. (5) we would expect the ratio of the proton and antiproton phase densities to be flat as a function of p_T. Fitting a constant to $\langle f_{\bar{p}} \rangle / \langle f_p \rangle$ yields a χ^2/NDF of 5.0/6 and 13.3/6 at $y = 0$ and $y = 0.8$, respectively. Near $y = 0$ the antiprotons have a slightly smaller value of space-averaged

TABLE I. Proton and deuteron yields, dN/dy, and inverse slopes T (MeV) derived from fitting spectra. The lower rows at rapidities $y = 0$ and $y = 0.8$ are for the antiparticles. The errors listed are statistical only. For dN/dy, the systematic errors due to extrapolation to low p_T is 5%–10% with an additional 8% from normalization and various corrections. The systematic errors on the inverse slope are less than 10%.

	Proton			Deuteron		
y	p_T Fit	dN/dy	T MeV	p_T Fit	dN/dy	T MeV
0.0	0.7–4.0	27.9(0.1)	354(2)	1.5–3.3	0.093(0.008)	570(70)
		20.8(0.1)	352(1)		0.033(0.004)	870(220)
0.8	0.5–4.0	26.0(0.1)	356(1)	1.5–3.3	0.068(0.003)	610(30)
		17.9(0.1)	361(1)		0.031(0.002)	700(80)
2.0	0.5–3.0	20.9(0.2)	314(3)	0.8–2.8	0.082(0.011)	460(110)
3.0	0.5–4.0	23.4(0.1)	282(1)	2.5–3.5	$0.25^{+0.30}_{-0.08}$	310(90)

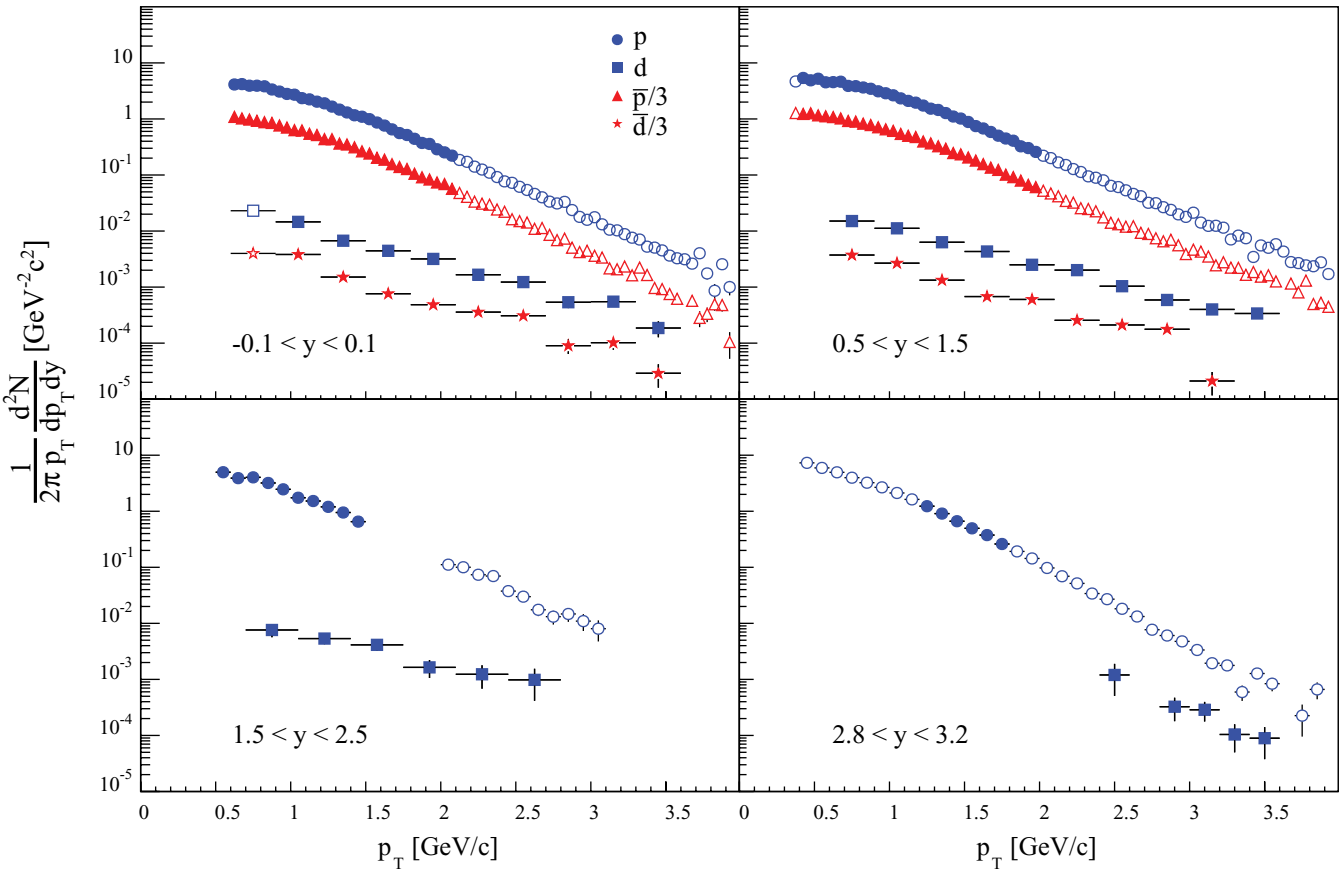

FIG. 3. (Color online) (Anti)Proton and (anti)deuteron p_T spectra at various rapidities for the top 20% most central Au + Au collisions. The filled-symbol part of the spectra show the p_T intervals used in the coalescence analysis. Note that the limits for the deuteron range are exactly twice those used for the protons. The errors are statistical only. The horizontal bars represent the bin width.

phase-space density compared to that of protons, suggesting a small chemical potential. At $\sqrt{s_{\rm NN}} = 17.3$ GeV the antiproton space-averaged phase-space density was 38 times smaller [13], which suggests a much larger baryochemical potential at the lower energy. The inverse slope derived from the space-averaged phase-space density is $T = 930 \pm 110$ MeV for protons. This is consistent with data at $\sqrt{s_{\rm NN}} = 17.3$ GeV, but much higher than the value extracted at $\sqrt{s_{\rm NN}} = 4.9$ GeV where the inverse slope is about 350 MeV (see Fig. 6). It should be noted that the proton, kaon and pion spectra at midrapidity can be well described by blast-wave fits, which suggest that this increase in the inverse slope with $\sqrt{s_{\rm NN}}$ is largely driven by an increase in radial flow. This is supported by the fact that the phase-density of pions is characterized by a much smaller inverse slope ($\approx$140 MeV) than that of protons [13].

Figures 4 and 5 imply that the volume of homogeneity, $\sim 1/B_2$, and the space-averaged phase-space density vary little with rapidity at $\sqrt{s_{\rm NN}} = 200$ GeV. This is in stark contrast to the situation at lower energy. Table II shows the rapidity dependence of B_2 and the space-averaged phase-space density at $p_T = 0$ for central Pb + Pb collisions at $\sqrt{s_{\rm NN}} = 17.3$ GeV [13,25,27]. These data are compared to BRAHMS results at $p_T/A = 1.3$ GeV/c, which show very little rapidity dependence. Finally, Fig. 6 shows the evolution of the space-averaged phase-space density near midrapidity as the energy of the system grows from AGS to RHIC values. The space-averaged phase-space density of protons decreases with

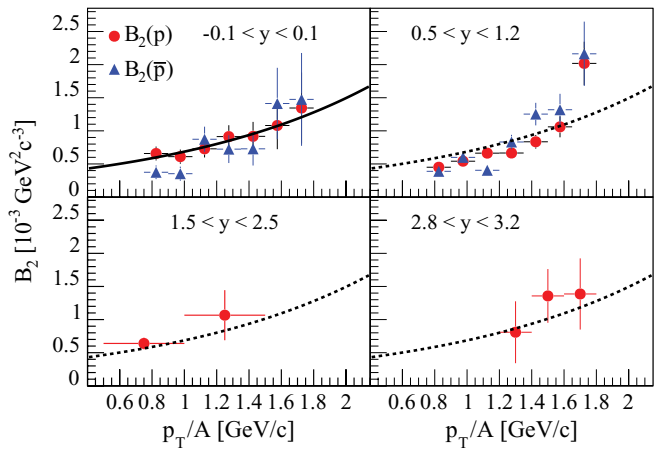

FIG. 4. (Color online) B_2 versus transverse momentum per nucleon at several rapidities for central Au + Au collisions at $\sqrt{s_{\rm NN}} =$ 200 GeV. Protons are displayed with filled circles and antiprotons with filled triangles. The solid line in the top-left panel is an exponential fit to the data at $y = 0$. This same line is shown, in dotted form, in the other three panels. The errors are statistical only.

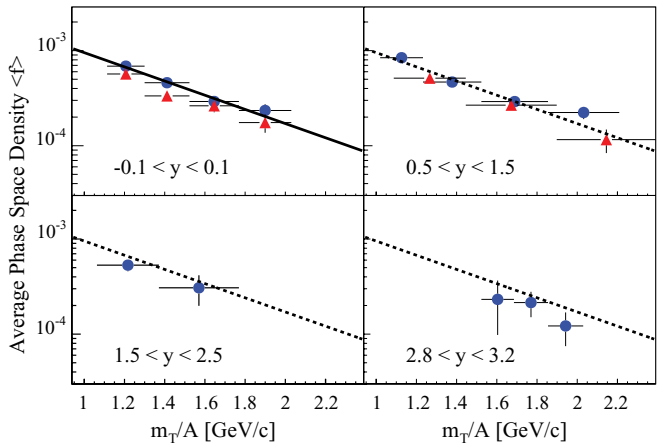

FIG. 5. (Color online) (Anti)Proton space-averaged phase-space density $\langle f \rangle (m_T/A)$ for central $\sqrt{s_{NN}} = 200$ GeV Au + Au collisions at several rapidities. The solid line in the top-left panel is an exponential fit to the data at $y = 0$. This same line is shown, in dotted form, in the other three panels. The errors are statistical only.

energy while that of antiprotons increases. At AGS energies, $\langle f \rangle$ at $m_T = 0$ is 10 times bigger than its value at RHIC, while at SPS it is 2 times bigger. In contrast, the pion average phase-space density has the opposite behavior as the energy of the colliding system increases; the values at RHIC [39] are higher than those at SPS by a factor ~2 where $\langle f \rangle = 0.45$ [55]. At $\sqrt{s_{NN}} = 4.9$ GeV, $\langle f \rangle$ was extracted from HBT and from spectra measured at high rapidity $\langle y \rangle \sim 3.1$ in Au + Au 10% central collisions, and its estimated value at midrapidity is ~5 times smaller that the RHIC value [22]. For antiprotons the growth in $\langle f \rangle$ is similar to that of pions. The different trend

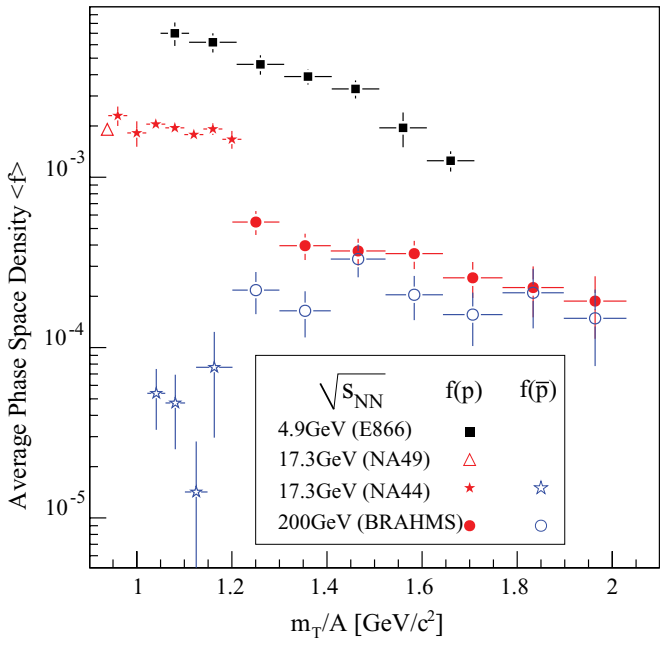

FIG. 6. (Color online) Proton space-averaged phase-space density for central collisions as a function of $\sqrt{s_{NN}}$ and m_T at $y = 0$ [13,23,26,27]. The errors are statistical only.

TABLE II. The rapidity dependence of B_2 and the f for (top) Pb + Pb collisions at $\sqrt{s_{NN}} = 17.3$ GeV and (bottom) $\sqrt{s_{NN}} = 200$ GeV Au + Au collisions. For the 17.3-GeV data the centrality is 23% at $y = 0.2$ [27] and 20% at $y = 0.8$ and 1.3 [13,25].

	$p_T/A = 0$			
	$y = 0.2$	$y = 0.8$	$y = 1.3$	
$B_2 \times 10^4$	7.9 ± 0.8	8.1 ± 0.3	13.7 ± 2.7	
$f \times 10^3$	1.9 ± 0.1	2.5 ± 0.2	3.3 ± 0.3	
	$p_T/A = 1.3$ GeV/c			
	$y = 0.0$	$y = 0.8$	$y = 2.0$	$y = 3.0$
$B_2 \times 10^4$	8.1 ± 1.0	6.6 ± 0.6	10.6 ± 0.4	8.1 ± 0.5
$f \times 10^4$	3.6 ± 0.6	2.4 ± 0.3	3.1 ± 1.0	2.3 ± 1.0

for the protons may be driven mainly by baryon transport; at AGS, most of the beam protons end up at midrapidity, less so at SPS, and at RHIC less than 10% of the beam protons are transported to midrapidity. The proton rapidity loss adds beam protons to the Gaussian rapidity density of produced protons and transforms the overall proton rapidity density into a flat distribution.

IV. SUMMARY

The rapidity dependence of the deuteron production in 0%–20% central Au + Au collisions at 200 GeV has been studied in the context of coalescence models. Near central rapidity the proton and antiproton phase-space densities are very similar, suggesting a small baryon chemical potential. The coalescence parameters, or B_2 values, for deuterons and antideuterons are also very close, suggesting similar freeze-out volumes for protons and antiprotons. B_2 increases with p_T, as expected for a system undergoing transverse flow; flow introduces a correlation between position and momentum. At a given p_T the deuteron coalescence parameter B_2 is independent of rapidity, which would imply that the homogeneity volume for protons of a given p_T is almost constant from $y = 0$ to $y = 3$. Baryon transport in these colliding systems may be affecting the rapidity density of protons. It is interesting to note that the radial flow varies weakly with rapidity [54]. The weak dependence of radial flow on rapidity offers an explanation of why the p_T dependence of B_2 does not depend on rapidity. It does not, however, address the fact that the overall magnitude of B_2 is constant from $y = 0$ to $y = 3$. The proton space-averaged phase-space density also shows no significant rapidity dependence, whereas it depends strongly on m_T and $\sqrt{s_{NN}}$. The space-averaged phase-space density can be thought of as the ratio of the number of protons per unity rapidity over the volume of the proton source. The rapidity density of protons decreases by only a factor of 0.84 ± 0.01 from $y = 0$ to $y = 3$. The constancy of the space-averaged phase-space density in rapidity is consistent with the similar behavior found for B_2. Thus we observe a striking invariance of the proton source over several units of rapidity.

ACKNOWLEDGMENTS

This work was supported by the Division of Nuclear Physics of the Office of Science of the US Department of Energy under contracts DE–AC02–98–CH10886, DE–FG03–93–ER40773, DE–FG03–96–ER40981, and DE–FG02–99–ER41121, the Danish Natural Science Research Council, the Research Council of Norway, the Polish Ministry of Science and Higher Education (Contract No. 1248/B/H03/2009/36), and the Romanian Ministry of Education and Research Grant No. 81-049/2007 (REEHUC). We thank the staff of the Collider-Accelerator Division at BNL for their excellent and dedicated work to deploy RHIC and their support to the experiment.

[1] BRAHMS Collaboration, I. Arsene *et al.*, Nucl. Phys. A **757**, 1 (2005); PHOBOS Collaboration, B. B. Back *et al.*, *ibid.* **757**, 28 (2005); STAR Collaboration, J. Adams *et al.*, *ibid.* **757**, 102 (2005); PHENIX Collaboration, K. Adcox *et al.*, *ibid.* **757**, 184 (2005).

[2] B. L. Ioffe, I. A. Shushpanov, and K. N. Zyablyuk, Int. J. Mod. Phys. E **13**, 1157 (2004).

[3] S. Leupold and U. W. Heinz, Phys. Rev. C **50**, 1110 (1994).

[4] S. Butler and C. Pearson, Phys. Rev. **129**, 836 (1963).

[5] J. Kapusta, Phys. Rev. C **21**, 1301 (1980).

[6] A. Z. Mekjian, Phys. Rev. C 1051 (1978); Nucl. Phys. A **312**, 491 (1978).

[7] L. R. Csernai and J. I. Kapusta, Phys. Rep. **131**, 223 (1986).

[8] E864 Collaboration, T. A. Armstrong *et al.*, Phys. Rev. C **60**, 064903 (1999).

[9] E866 Collaboration, E. L. Ahle *et al.*, Nucl. Phys. A **610**, 139c (1996).

[10] E877 Collaboration, R. Lacasse *et al.*, Nucl. Phys. A **610**, 153c (1996).

[11] B. K. Jennings, S. Das Gupta, and N. Mobed, Phys. Rev. C **25**, 278 (1982).

[12] W. J. Llope *et al.*, Phys. Rev. C **52**, 2004 (1995).

[13] M. Murray and B. Holzer, Phys. Rev. C **63**, 054901 (2001).

[14] P. E. Hodgson, *Nuclear Reactions and Nuclear Structure* (Clarendon-Press, Oxford, 1971), p. 453.

[15] H. Gutbrod *et al.*, Phys. Rev. Lett. **37**, 667 (1976); S. Nagamiya, M. C. Lemaire, E. Moeller, S. Schnetzer, G. Shapiro, H. Steiner, and I. Tanihata, Phys. Rev. C **24**, 971 (1981); B. V. Jacak, D. Fox, and G. D. Westfall, *ibid.* **31**, 704 (1985).

[16] J. W. Cronin, H. J. Frisch, H. J. Frisch, J. P. Boymond, R. Mermod, P. A. Piroue, and R. L. Sumner, Phys. Rev. D **11**, 3105 (1975).

[17] E886 Collaboration, N. Saito *et al.*, Phys. Rev. C **49**, 3211 (1994).

[18] A. Bussiere *et al.*, Nucl. Phys. B **174**, 1 (1980).

[19] E864 Collaboration, T. A. Armstrong *et al.*, Phys. Rev. Lett. **85**, 2685 (2000).

[20] E864 Collaboration, T. A. Armstrong *et al.*, Phys. Rev. C **61**, 064908 (2000).

[21] M. Aoki *et al.*, Phys. Rev. Lett. **69**, 2345 (1992).

[22] E877 Collaboration, J. Barrette *et al.*, Phys. Rev. Lett. **78**, 2916 (1997).

[23] E866 Collaboration, L. Ahle *et al.*, Phys. Rev. C **60**, 064901 (1999); **57**, R466 (1998).

[24] E896 Collaboration, S. Albergo *et al.*, Phys. Rev. C **65**, 034907 (2002).

[25] NA44 Collaboration, I. G. Bearden *et al.*, Eur. Phys. J. C **23**, 237 (2002).

[26] NA44 Collaboration, I. G. Bearden *et al.*, Phys. Rev. Lett. **85**, 2681 (2000).

[27] NA49 Collaboration, T. Anticic *et al.*, Phys. Rev. C **69**, 024902 (2004).

[28] PHENIX Collaboration, S. S. Adler *et al.*, Phys. Rev. Lett. **94**, 122302 (2005).

[29] PHENIX Collaboration, S. Afanasiev *et al.*, Phys. Rev. Lett. **99**, 052301 (2007).

[30] STAR Collaboration, B. I. Abelev *et al.*, arXiv:0909.0566.

[31] S. Das Gupta and A. Z. Mekjian, Phys. Rep. **72**, 131 (1981).

[32] H. Sato and K. Yazaki, Phys. Lett. B **98**, 153 (1981).

[33] Rüdiger Scheibl and Ulrich Heinz, Phys. Rev. C **59**, 1585 (1999).

[34] STAR Collaboration, C. Adler *et al.*, Phys. Rev. Lett. **87**, 262301 (2001).

[35] PHENIX Collaboration, S. S. Adler *et al.*, Phys. Rev. Lett. **94**, 122302 (2005).

[36] PHENIX Collaboration, S. S. Adler *et al.*, Phys. Rev. Lett. **93**, 152302 (2004).

[37] STAR Collaboration, J. Adams *et al.*, Phys. Rev. C **71**, 044906 (2005).

[38] G. F. Bertsch, Phys. Rev. Lett. **72**, 2349 (1994); **77**, 789 (1996).

[39] S. Pal and S. Pratt, Phys. Lett. B **578**, 310 (2004).

[40] B. Tomasik and U. W. Heinz, Phys. Rev. C **65**, 031902 (2002).

[41] M. J. Murray, J. Phys. G **28**, 2069 (2002).

[42] NA44 Collaboration, H. Bøggild *et al.*, Phys. Lett. B **458**, 181 (1999).

[43] NA44 Collaboration, H. Beker *et al.*, Phys. Rev. Lett. **74**, 3340 (1995).

[44] NA44 Collaboration, I. G. Bearden *et al.*, Phys. Rev. Lett. **87**, 112301 (2001).

[45] R. Debbe *et al.*, Nucl. Instrum. Methods A **570**, 216 (2007).

[46] BRAHMS Collaboration, M. Adamczyk *et al.*, Nucl. Instrum. Methods A **499**, 437 (2003).

[47] Y. K. Lee, R. Debbe, J. H. Lee, H. Ito, and S. J. Sanders, Nucl. Instrum. Methods A **516**, 281 (2004).

[48] BRAHMS Collaboration, I. G. Bearden *et al.*, Phys. Rev. Lett. **88**, 202301 (2002).

[49] GEANT CERN Program Library.

[50] BRAHMS Collaboration, I. Arsene *et al.*, Phys. Rev. C **72**, 014908 (2005).

[51] BRAHMS Collaboration, I. G. Bearden *et al.*, Phys. Rev. Lett. **93**, 102301 (2004).

[52] PHENIX Collaboration, K. Adcox *et al.*, Phys. Rev. Lett. **89**, 092302 (2002).

[53] L. A. Stiles and M. Murray, arXiv:nucl-ex/0601039.

[54] BRAHMS Collaboration, S. J. Sanders *et al.*, Nucl. Phys. A **830**, 179C (2009).

[55] D. Ferenc, U. Heinz, B. Tomasik, U. A. Wiedemann, and J. G. Cramer, Nucl. Phys. A **661**, 374 (1999).